LANGLEY GRANT
IN-36-CR
234873

L32

# High Resolution Doppler Lidar

## Final Report

Submitted to:
National Aeronautics and Space Administration

NASA Grant
NAG1-817

Prepared by:

Vincent J. Abreu
Paul B. Hays
John E. Barnes

Space Physics Research Laboratory
The University of Michigan
Department of Atmospheric, Oceanic and Space Sciences
Ann Arbor, MI 48109-2143

October 1989

(NASA-CR-183288) HIGH RESOLUTION DOPPLER LIDAR Final Report (Michigan Univ.) 32 p
CSCL 20E

N90-14542

Unclas
G3/36 0234873

# High Resolution Doppler Lidar

## Final Report

Submitted to:
National Aeronautics and Space Administration

NASA Grant
NAG1-817

Prepared by:

Vincent J. Abreu
Paul B. Hays
John E. Barnes

Space Physics Research Laboratory
The University of Michigan
Department of Atmospheric, Oceanic and Space Sciences
Ann Arbor, MI 48109-2143

October 1989

## *I. INTRODUCTION*

Ground based incoherent lidar systems working in the blue-green wavelength region (0.5μ) have been demonstrated to have the capability of measuring the vector wind from the ground with an accuracy exceeding one meter per second (Benedetti-Michelangeli et al., 1972; 1974). This technique of determining the wind velocity relies on detecting the doppler shift experienced by a pulse of narrow band laser light as it is scattered by the molecular and aerosol components of the atmosphere. The detection is done using an incoherent interferometric determination of the laser wavelength before and after scattering. The Space Physics Research Laboratory (SPRL) has implemented a ground-based incoherent lidar system as a prototype of a space-borne lidar. This is a stable, high resolution system consisting of an optically contacted plane etalon, and a multi-ring anode detector to spatially scan the image plane of the Fabry-Perot. The high resolution provided by the interferometer allows the separation of the aerosol and molecular components of the backscattered signal. The doppler shift of the aerosol component is then used to determine the line of sight wind altitude profile in the troposphere and stratosphere. In this report we describe the High Resolution Doppler Lidar (HRDL) developed at SPRL, and present the system characteristics and sample measurements.

## *II. INSTRUMENT DESCRIPTION*

The design of the HRDL is based on the experience accumulated by the engineering and scientific staff at the Space Physics Research Laboratory from several programs including the Dynamics Explorer Fabry-Perot Interferometer (Hays et al., 1981), the ground based Michigan Airglow Observatory (Meriwether et al., 1984) and the Upper Atmosphere Research Satellite High Resolution Doppler Imager. These programs have provided a basis in Fabry-Perot technology including highly stable etalons capable of wavelength determination with image plane detector photomultiplier tubes. The design of the HRDL was also based on a number of incoherent lidar studies (Abreu et al., 1979, 1980, 1981; Hays et al., 1984), aimed at determining system parameters which optimize the measurement.

The High Resolution Doppler Lidar system is located on the second floor of the SPRL building under a removable dome which allows viewing directly overhead. Except for the telescope, the system is mounted on a four foot by six foot optical bench. Figure II.1 shows a block diagram of the HRDL set up. The three basic components of the HRDL are the transmitting, the receiving, and the data acquisition and control systems. The

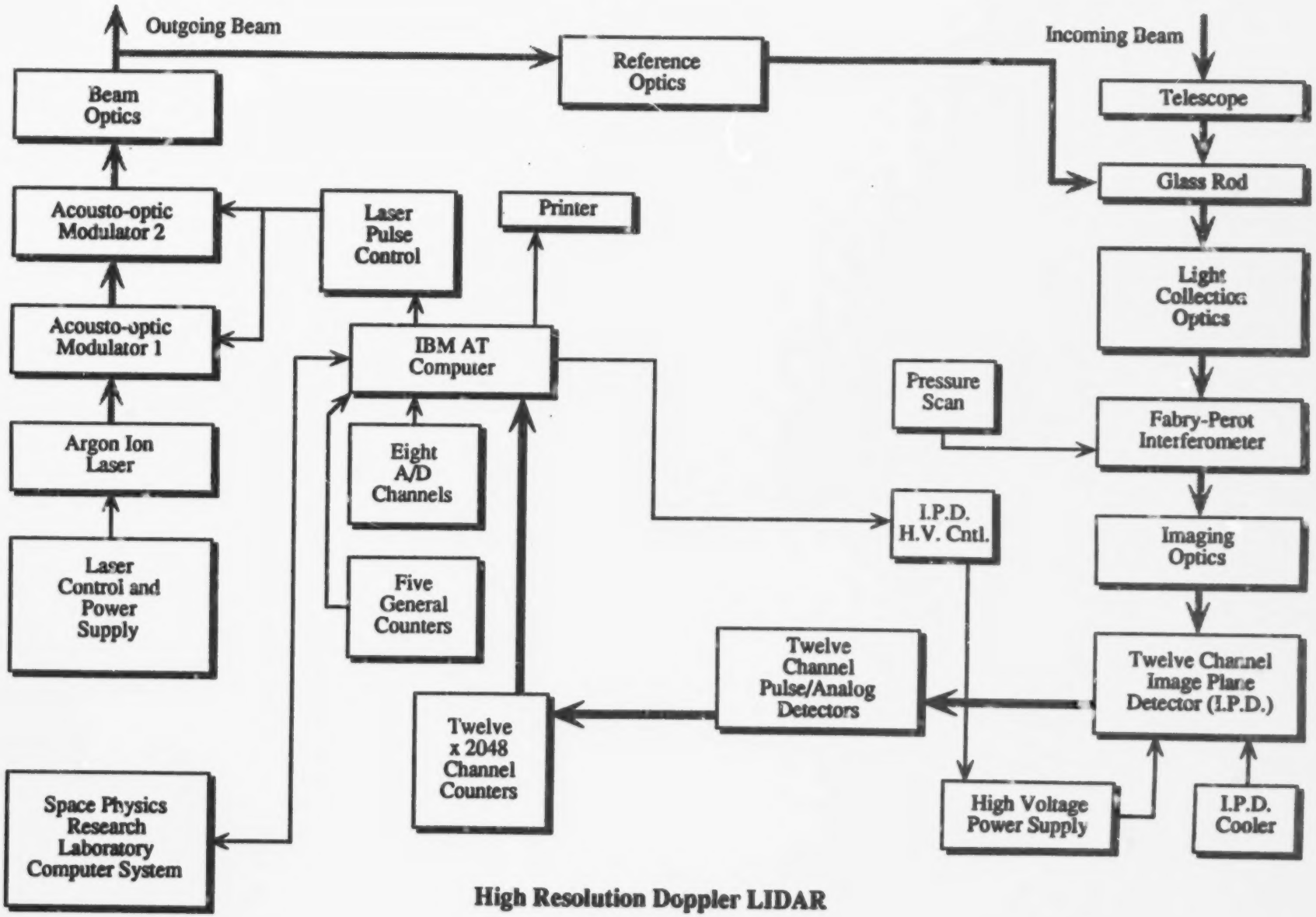


**High Resolution Doppler LIDAR**

Figure II.1

transmitting system consists of a cw laser and two acousto-optic modulators. The Fabry-Perot/detector system is the core of the receiving system, which also includes a telescope. The telescope feeds the scattered signal to an interferometer that determines doppler shifts in the signal. The ring pattern from the interferometer is detected by a 12 channel photomultiplier image plane detector (IPD) whose signal is amplified by a high speed pulse analog detector (PAD), and sent to the computer. The computer fires the laser multiple times and integrates the signal using digital hardware. Each of these components will be described next.

*Transmitting System*

A schematic showing the details of the transmitting system is shown in Figure II.2. The light source used here is a Coherent Model INNOVA 100, Argon Ion laser, operating in the green at a wavelength of 514 nanometers. Table I describes the basic properties of this laser. In continuous single mode operation the power output of the laser is seven watts. The laser beam is pulsed using acousto-optic modulators (AOM). The transmission of each modulator at the wavelength of interest is ~98%. Two modulators are used serially to improve the extinction of the beam in the off mode. With the two AOMs the ratio of the power on to power off is $\sim 10^6$. Both modulators have modulation efficiencies greater than 85%, and rise/fall times ~10 nanoseconds. The rise/fall time determines the ultimate altitude resolution attainable by limiting the minimum length of the laser pulse. In this system the receiving electronics limit the pulse length to a minimum of 25 nanoseconds. In actuality the altitude resolution is limited by the signal to noise. The properties of the AO modulators are summarized in Table II. The lens labelled L3 in Figure II.2 has been designed to increase the divergence of the laser beam to an optimum value of 0.5 milliradian.

The return signal from the lidar system depends upon the overlap of the laser beam, the field of view of the receiver telescope, and the geometry of the telescope aperture. The transmitting beam overlap with the viewing angle of the telescope is accomplished by changing the direction of the exiting laser beam with the final mirror (M) shown in Figure II.2.

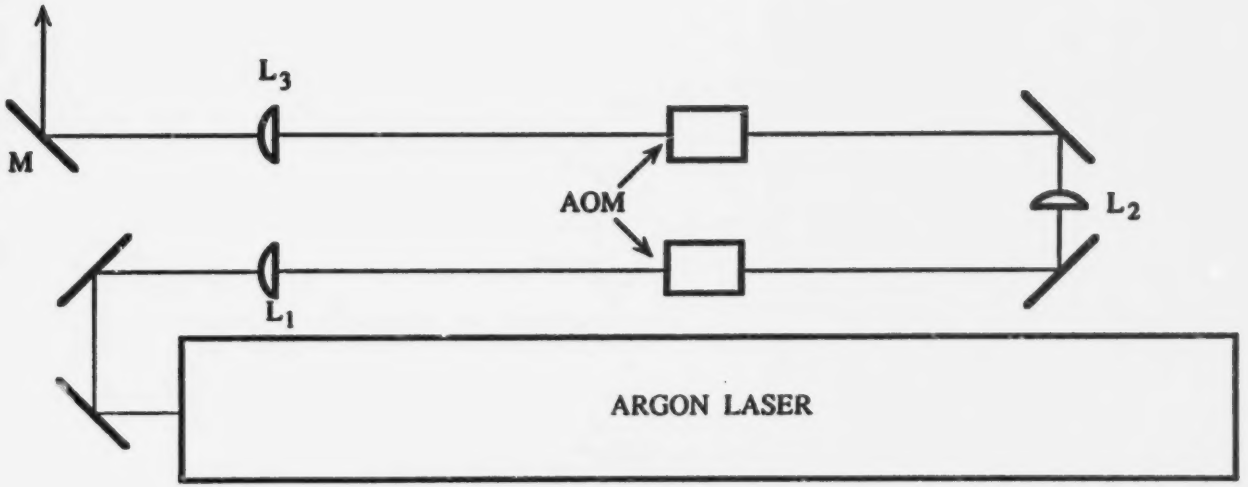


**LASER MODULATION SYSTEM**

| | Diameter (mm) | Focal Length (mm) |
|---|---|---|
| $L_1$ | 25.4 | 750 |
| $L_2$ | 25.4 | 300 |
| $L_3$ | 25.4 | 750 |

Figure II.2

| TABLE I<br>LASER PARAMETERS | |
|---|---|
| Manufacturer: | Coherent, Model INNOVA 100 |
| Beam Diameter: | 1.9 mm |
| Beam Divergence: | 0.39 mrad<br>0.50 mrad - outgoing |
| Long Term Stability: | ± 0.5% |
| Optical Noise: | 0.3% RMS<br>(10 Hz – 2 MHz bandwidth) |
| Single Mode Line Width: | ≈ 50 MHz |
| Intercavity Etalon Spacing: | ~ 150 MHz |
| Max Power: | 7 watts in single mode |

| TABLE II<br>ACOUSTO-OPTIC MODULATOR | |
|---|---|
| Manufacturer: | Newport, Model# N31085-605 |
| Description: | High power $S_iO_2$ modulator<br>(250 watt) |
| Transmission: | 98% at 514 nm |
| Efficiency: | 85% at 514 nm |
| Frequency: | 85.019 MHz |
| Rise/Fall time: | 9 nsec / 5 nsec |
| Extinction Ratio: | 60 db |

*Receiving System*

The components of the detection system are shown in Figure II.3. All components, except for the telescope, are mounted on a 2 foot by 6 foot optical bench which is positioned vertically on the main optical bench. Mounting the etalon in a vertical position (plates parallel to the floor) improves its performance. The backscattered signal is received by an Odyssey 2, 44.5 cm, f/4.5, Newtonian Astronomical telescope on a Dobsonian mount. The field of view of the telescope has been matched to the beam divergence of the final

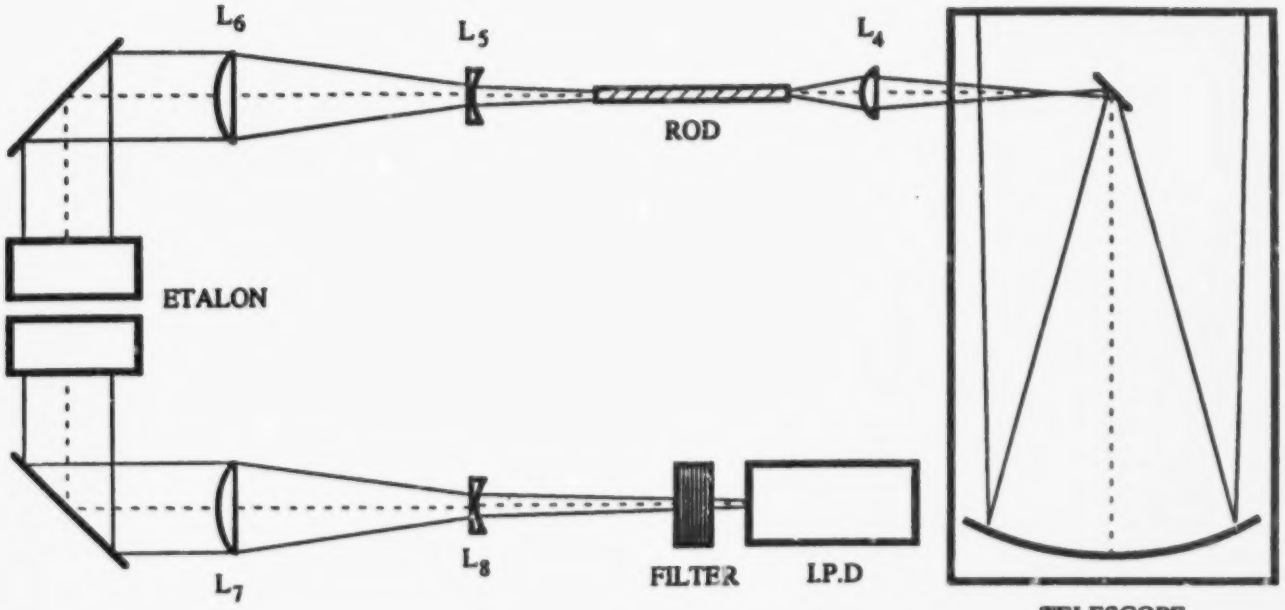


| | Diameter (mm) | Focal Length (mm) |
|---|---|---|
| Telescope | 444 | 2000 |
| $L_4$ | 25.4 | 25.4 |
| $L_5$ | 50.8 | -150 |
| $L_6$ | 100 | 500 |
| Etalon | 96 | — |
| $L_7$ | 100 | 500 |
| $L_8$ | 50.8 | -150 |
| Filter | 25.4 | — |
| I.P.D. | 12.0 | — |

**LIDAR DETECTION SYSTEM**

Figure II.3

modulated laser pulse. This field of view is then imaged onto a 3 mm diameter glass rod which serves to "scramble" any spatial variations in intensity that are imaged by the telescope. The spatial variations are created by the Gaussian beam profile of the modulated laser light which illuminates the atmosphere with the same profile in intensity, and by inhomogeneity in the distribution of scatterers.

Following the glass rod, the light is collimated by a telephoto lens pair (effective focal length = 66 cm) into the Fabry-Perot etalon. The etalon has a diameter of 9.6 cm. and a plate separation of 10 cm. This determines an angle of two milliradians for one free spectral range, which corresponds to a wind speed of 300 meters per second. The measured finesse of the etalon and imaging optics is approximately 14. The temperature of the etalon is regulated for stability and the etalon can also be pressure scanned.

The ring pattern from the Fabry-Perot etalon is imaged by a second telephoto lens pair (effective focal length = 264 cm) onto the Image Plane Detector (IPD). The IPD geometry is matched to the ring pattern produced by a Fabry-Perot etalon. It is composed of twelve concentric ring anodes, each having equal areas, such that the spatial scan is linear in wavelength. The amplification of an arriving photon is accomplished by a micro-channel plate biased with respect to the anodes. Photons are counted on each of the twelve anodes simultaneously. The array of anodes is 1.2 cm in diameter and the detector is cooled to 263 K for reduction in thermal noise. The quantum efficiency of the detector is approximately 4.4%.

Data Acquisition and Control

The HRDL data acquisition and control system consists of three main electronic component sections. These are the control computer, the high speed pulse analog detector for the image plane detector, the shutter control circuit for the AO modulator.

The control computer is an IBM-AT clone operating at 8 Mhz. The system is shown in Figure II.4. In a multibus rack separate from the computer are the custom designed cards that control the timing of the laser firing and collecting of the 12 channels of data. This rack is connected to the AT by bus interface cards. This configuration makes data transfer from the bus to the AT very fast. There are two additional I/O cards within the multibus rack, which provide 8 channels of analog inputs, 5 channels of pulse counter input, 2 channels of time base pulse outputs, and 6 digital I/O channels.

The control card in the multibus rack operates the synchronization of detector gain, laser firing, acquisition timing, and data bin addressing. The operating sequence for the control card is shown in Figure II.5. In this design the electronics can independently cycle through

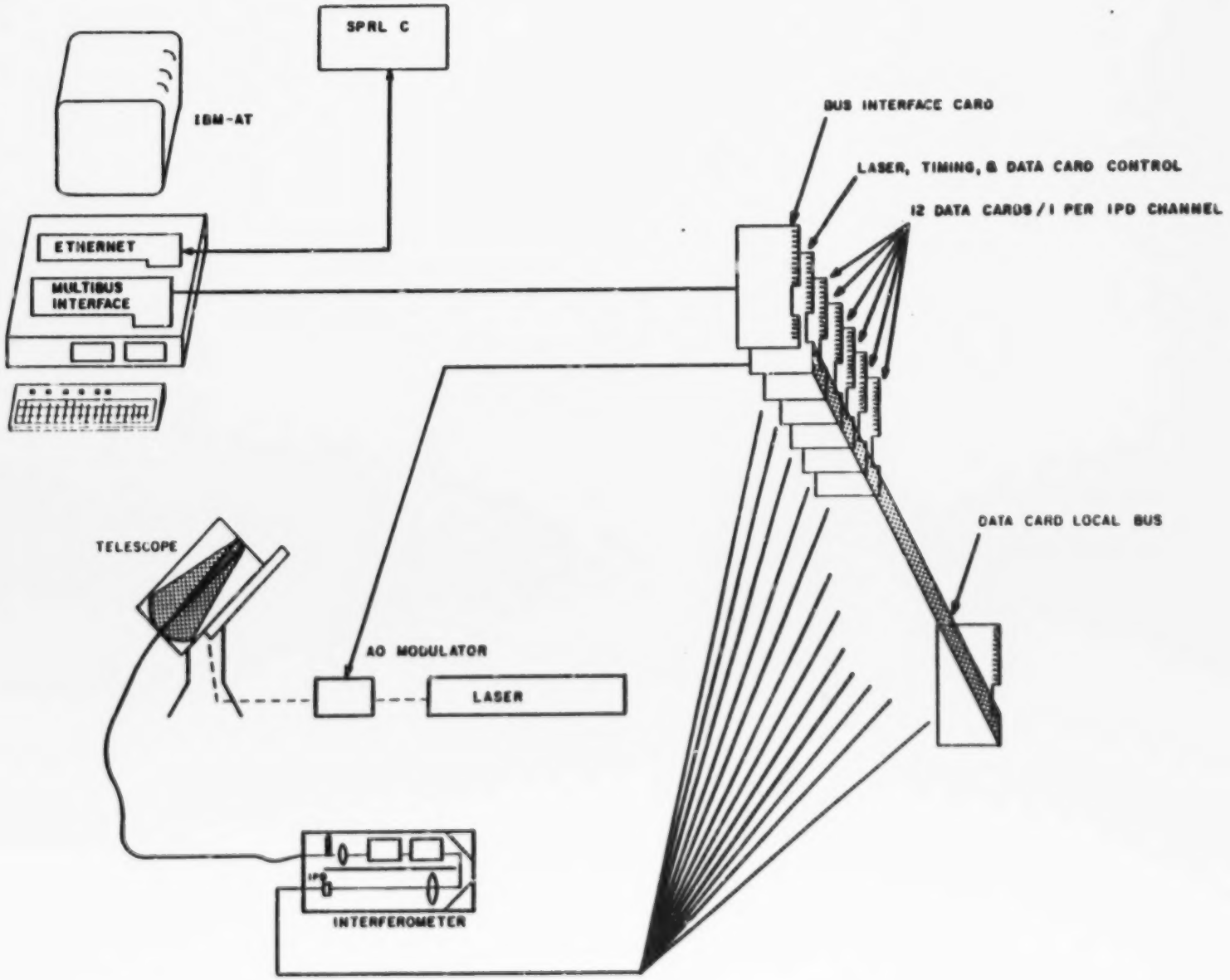
SPRL C
IBM-AT
ETHERNET
MULTIBUS INTERFACE
BUS INTERFACE CARD
LASER, TIMING, & DATA CARD CONTROL
12 DATA CARDS / 1 PER IPD CHANNEL
DATA CARD LOCAL BUS
TELESCOPE
AO MODULATOR
LASER
IPD
INTERFEROMETER

Figure II.4

CONTROL CARD

1. START DELAY
2. LASER PULSE WIDTH
3. END OF PULSE DELAY
4. IPD GAIN TIMING
5. NUMBER OF LASER PULSES
6. DATA RATE (A/D CLOCK)
7. DATA DURATION
8. DATA BOARD INTERFACE

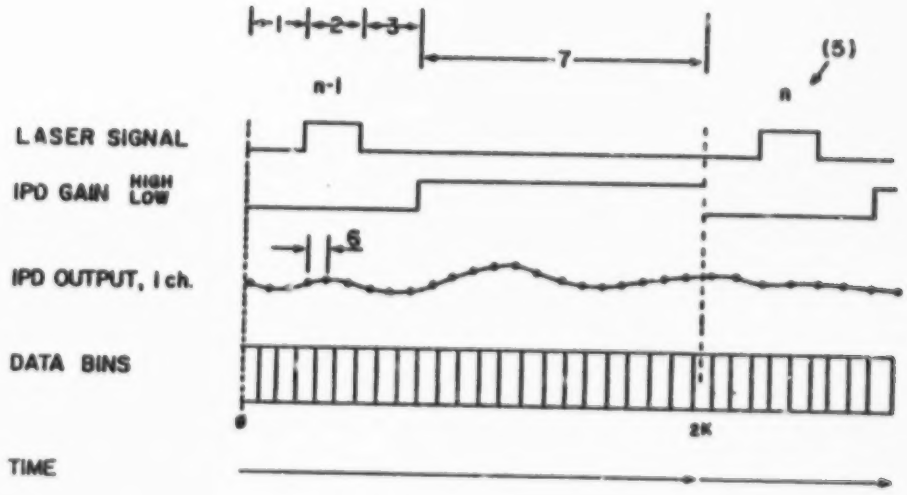


- START DELAY 400nS TO 1.6mS
- FIRE TIME 0nS TO 1.6mS
- DELAY WIDTH 0nS TO 1.6mS mSEC
- UP TO 65536 LASER PULSE INTEGRATION
- DATA RATE FROM 10 Mhz TO 40Khz (8 bit)
- DATA DURATION FROM 400 nS TO 16 mSEC
- DATA DURATION 2 MILLION INTEGRATIONS BEFORE OVERFLOW INTERRUPT

- ANALOG RESOLUTION 11 BITS AT 2 Mhz
- PULSE COUNTING RESOLUTION 11 BITS AT 50 Mhz

Figure II.5

the steps shown in the figure up to 65500 times. The laser is fired at a programmed time and for a chosen duration, while the returned photons are counted into successive bins. There are 12 data cards located in the multibus rack, one for each channel of the image plane detector. The data cards use a private bus to the control card that allows the passage of command and synchronization signals from the control card. The specifications for the data cards are given in Table III. The mode (analog acquisition or digital counting) is determined by the control card, and can be switched from analog to digital on the fly. All data cards work in unison under the command of the control card. The backscattered signal is binned in time, the time duration (period) of the bins being determined by the pulse length and the desired altitude resolution. The minimum resolution achievable is 1μsec, which corresponds to an altitude resolution of 150 m if viewing in the vertical direction. For every period, the data card will:

1. Perform an acquisition of either the flash A/D or the pulse counter.
2. Read the contents of an altitude bin pointed to by the control card's bin pointer.
3. Add the acquisition to the contents of the bin.
4. Write the results to the altitude bin.

**TABLE III**
**DATA CARD SPECIFICATIONS**

| | |
|---|---|
| Data bins: | 2048 bins each 32 bits deep; MSB reserver for overflow flag; 120 nSec memory |
| A/D: | 11 bit CMOS two-step flash converter |
| | 2 MHz conversion rate |
| | 0 - 1v input amplifier |
| | 75 ohm input impedance |
| | low noise input amplifier (0.4 mV rms noise) |
| | Conversion accuracy +/- 2 LSB |
| Counter: | 11 bit FAST counter (Fairchild Advanced Shottkey TTL) |
| | 50 mHz count rate |
| | 75 ohm input impedance |

The control card would then command the bin pointer to the next altitude bin and continue the data cards acquisiton cycle until the prescribed number of altitude bins have been read for a single laser firing. At the end of the laser firing cycle the bin pointer would be reset to the top of the altitude bin and the control card would start the next cycle. The control card can specify in a single command that up to 65500 laser firings be added. This process is very fast, since it is done independently of the computer.

The signals from the twelve IPD channels are amplified by charge sensitive preamplifiers. Their design is based on new, fast operational amplifiers available from Harris Semiconductors. The PAD circuit is capable of counting up to ~$10^7$ photoelectric events per second with IPD gains as low as $10^4$. The PAD will also be able to measure cathode current as the count rate increases beyond the IPD's capability to pulse count. This mode is useful when measuring the signal backscattered in the near field.

When the data acquisition electronics has finished, an integration period's data are stored, and the bins zeroed. Operational parameters are recorded as well as several channels of experimental values monitored by A/D conversion electronics. Continuous display of the data permits immediate preliminary analysis and provides a check on the status of the system. Data analysis is performed on a Vax 8600, which is part of the SPRL Network. The system has complete data analysis and graphics software available, as well as color graphics hardware.

## *III. INSTRUMENT PERFORMANCE*

### *Fabry-Perot /Detector Instrument Function*

The system finesse (etalon finesse and aperture finesse) has been measured for each of the twelve detector channels. The Coherent Innova 100 was used directly as a source. The measurement was carried out by pressure scanning the Fabry-Perot, while spatially recording the signal using the multi-ring detector. The pressure scans representing the Fabry-Perot/detector system instrument function are shown in Figure III.1 for selected channels. Table IV shows the finesse of each of the channels. It is obvious that the instrument function deteriorates toward the outer channels. This is a product of the coupling that occurs as the outer detector rings become narrower. This problem has been solved for the detector used on the High Resolution Doppler Imager to be flown in the UARS, by using an anti-coincidence circuit which decouples adjacent channels, and significantly improves the finesse of the outer channels.

**Table IV**

| Channel | Finesse | Channel | Finesse |
|---|---|---|---|
| 1 | 6.6268 | 7 | 2.9195 |
| 2 | 5.3873 | 8 | 2.4907 |
| 3 | 4.4020 | 9 | 2.5450 |
| 4 | 3.6864 | 10 | 2.4957 |
| 5 | 3.3383 | 11 | 2.0210 |
| 6 | 3.5626 | 12 | 2.2491 |

### *Optical Throughput*

The system optical transmission has been determined using a calibrated photodiode traceable to an NTB standard. The He-Ne laser was used to diffusely illuminate the glass rod, then the photodiode was used to measure the signal transmitted through the system (without the Fabry-Perot). The measured optical transmission was 25%.

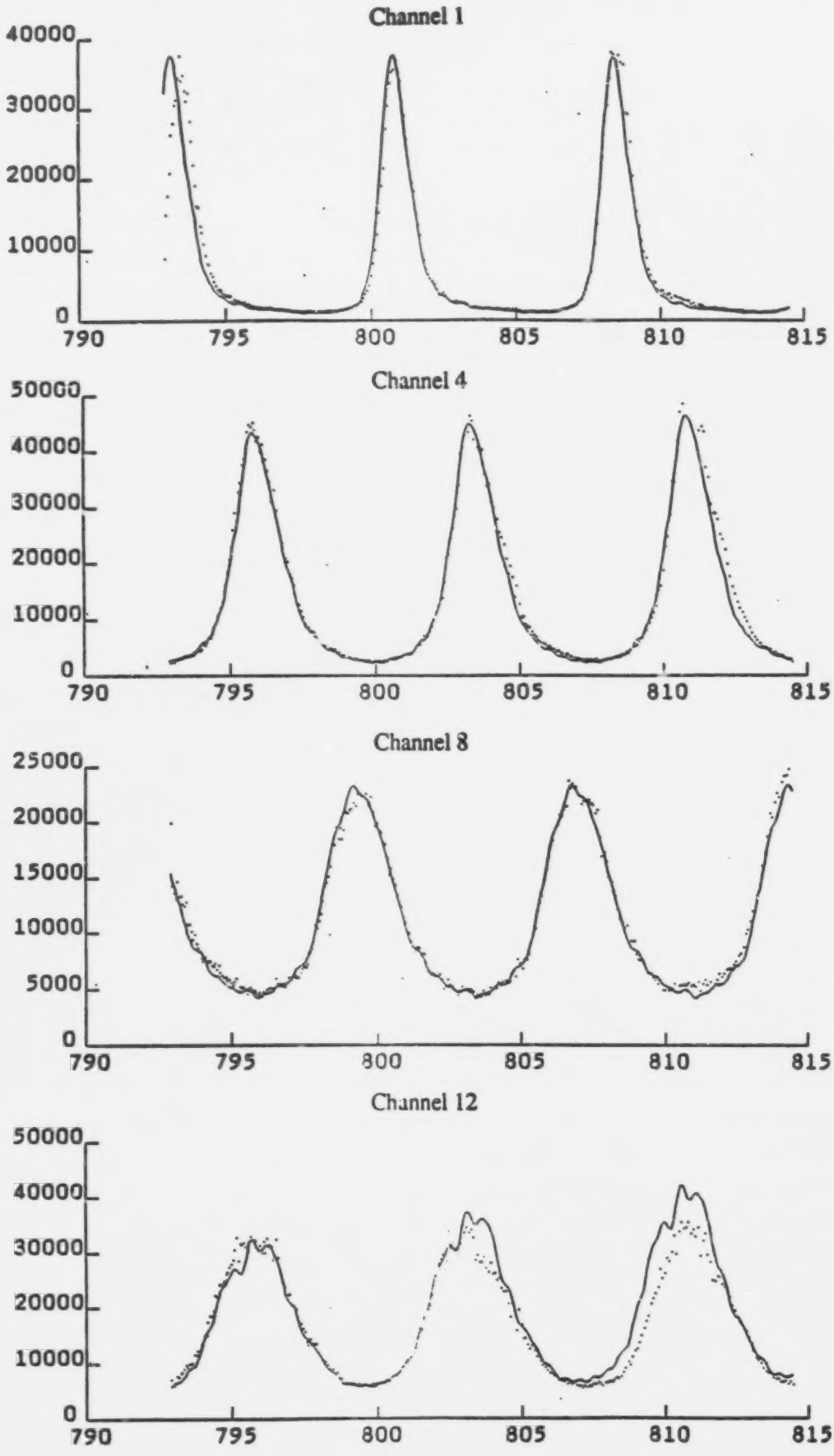
Channel 1
40000
30000
20000
10000
0
790
795
800
805
810
815
Channel 4
50000
40000
30000
20000
10000
0
790
795
800
805
810
815
Channel 8
25000
20000
15000
10000
5000
0
790
795
800
805
810
815
Channel 12
50000
40000
30000
20000
10000
0
790
795
800
805
810
815

Figure III.1

*Laser Wavelength Stability*

The Coherent Innova 100 provides a short time drift of the order of 1 m/s per 15 seconds, and consequently it is necessary to monitor the transmitted laser wavelength in order to accurately measure the wind speed. The interferometer has the ability to measure the exiting laser pulse wavelength. This process is shown in the schematic in Figure II.1, where a portion of the exiting beam is routed directly into the interferometer. The doppler shift of the backscattered signal is determined during data processing, and referenced to the position of the outgoing beam.

*Measurements*

In this section sample measurements of the lidar backscattered signal are presented. Measurements were carried out on August 9, 1989 with the laser beam pointed in the vertical direction. The laser pulses were 1μs (150 m) long, while the energy transmitted per pulse was $5 \times 10^{-6}$ joules (5 watts equivalent power). The data shown here is the average of $6.1 \times 10^6$ pulses, obtained over a time interval equal to 28.5 minutes with a 22% duty cycle. Figure III.2 shows the return in counts/s of the interferometer peak channel (channel 3), while Figure III.3 shows the twelve-channel detector output at selected altitudes. System simulations, presented in Figure III.4, show the simulated backscattered return convolved with the measured instrument function of the peak channel of the interferometer. Two cases are presented in this figure. The solid line represents the counts that would be observed if the receiving and transmitting systems were perfectly aligned, while the dashed line represents the counts as a function of altitude if a 1 milirad misalignment exist. The misaligned simulated signal agrees better with the measurement shown in figure III.2. The agreement is good, considering the fact that the aerosol and atmospheric models are unknown, lending confidence to the optimization and simulations carried out for a spaceborne lidar.

The aerosol backscattered signal observed is sharp and well suited for the wind analysis. The data analysis assumes that the measured signal is a Gaussian and consists of fitting three parameters to the measured signal: the peak intensity, the background, and the line of sight wind velocity. The data analysis is described in Appendix I. Figure III.5 shows the deduced line of sight wind. As expected the vertical wind is near zero. The measurements are shown up to ~3 km, where the signal to noise ratio decreases significantly and the error bars become large. Longer integration times or higher laser power allows the wind to be measured to higher altitude, and to higher accuracy.

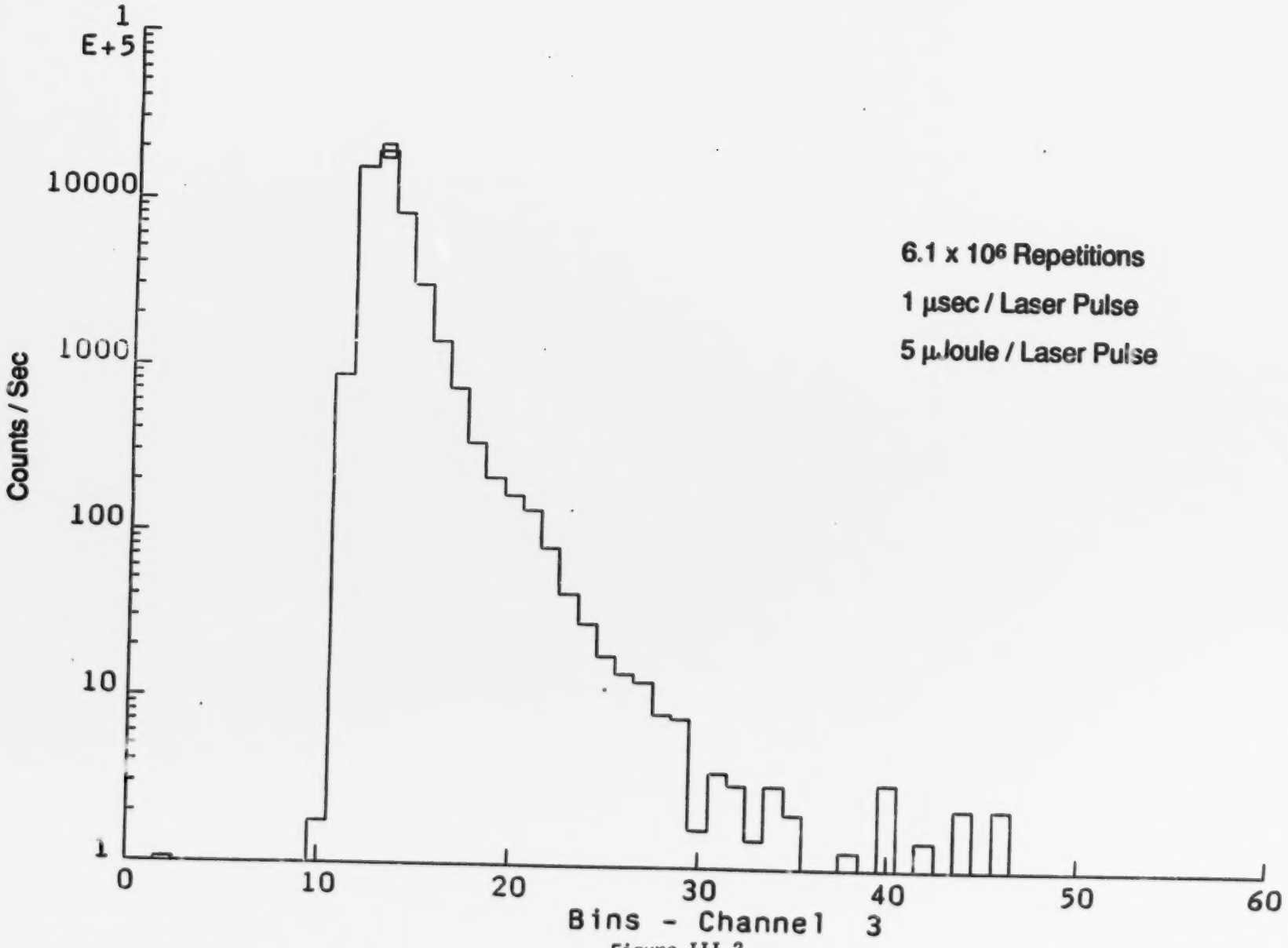
1
E+5
10000
1000
100
10
1
Counts / Sec
0
10
20
30
40
50
60
Bins - Channel 3
6.1 x 10⁶ Repetitions
1 μsec / Laser Pulse
5 μJoule / Laser Pulse

Figure III.2

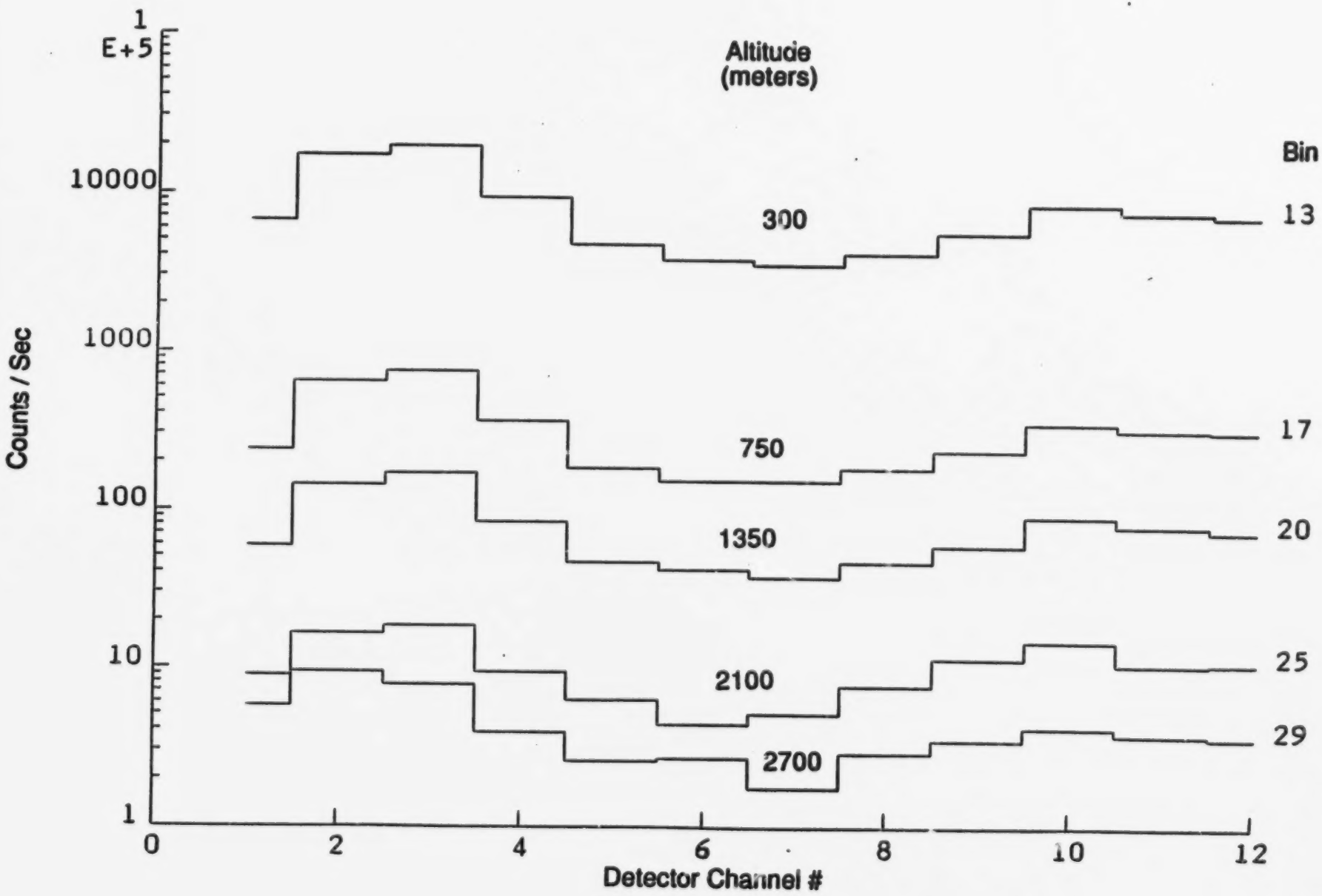
1
E+5
10000
1000
100
10
1
Counts / Sec
Altitude
(meters)
Bin
300
13
750
17
1350
20
2100
25
2700
29
0
2
4
6
8
10
12
Detector Channel #

Figure III.3

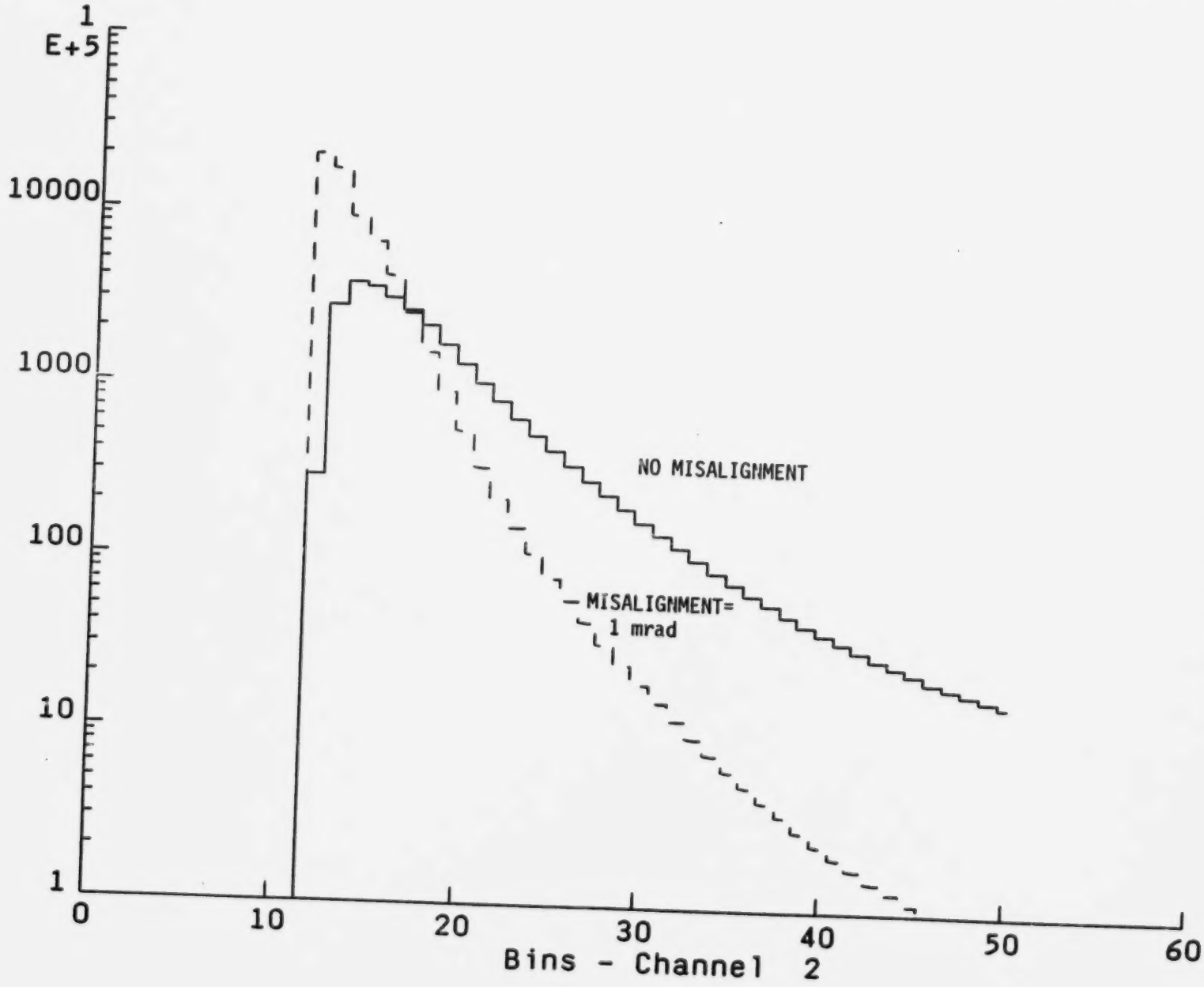
1
E+5
10000
1000
100
10
1
0
10
20
30
40
50
60
Bins - Channel 2
NO MISALIGNMENT
MISALIGNMENT=
1 mrad

Figure III.4

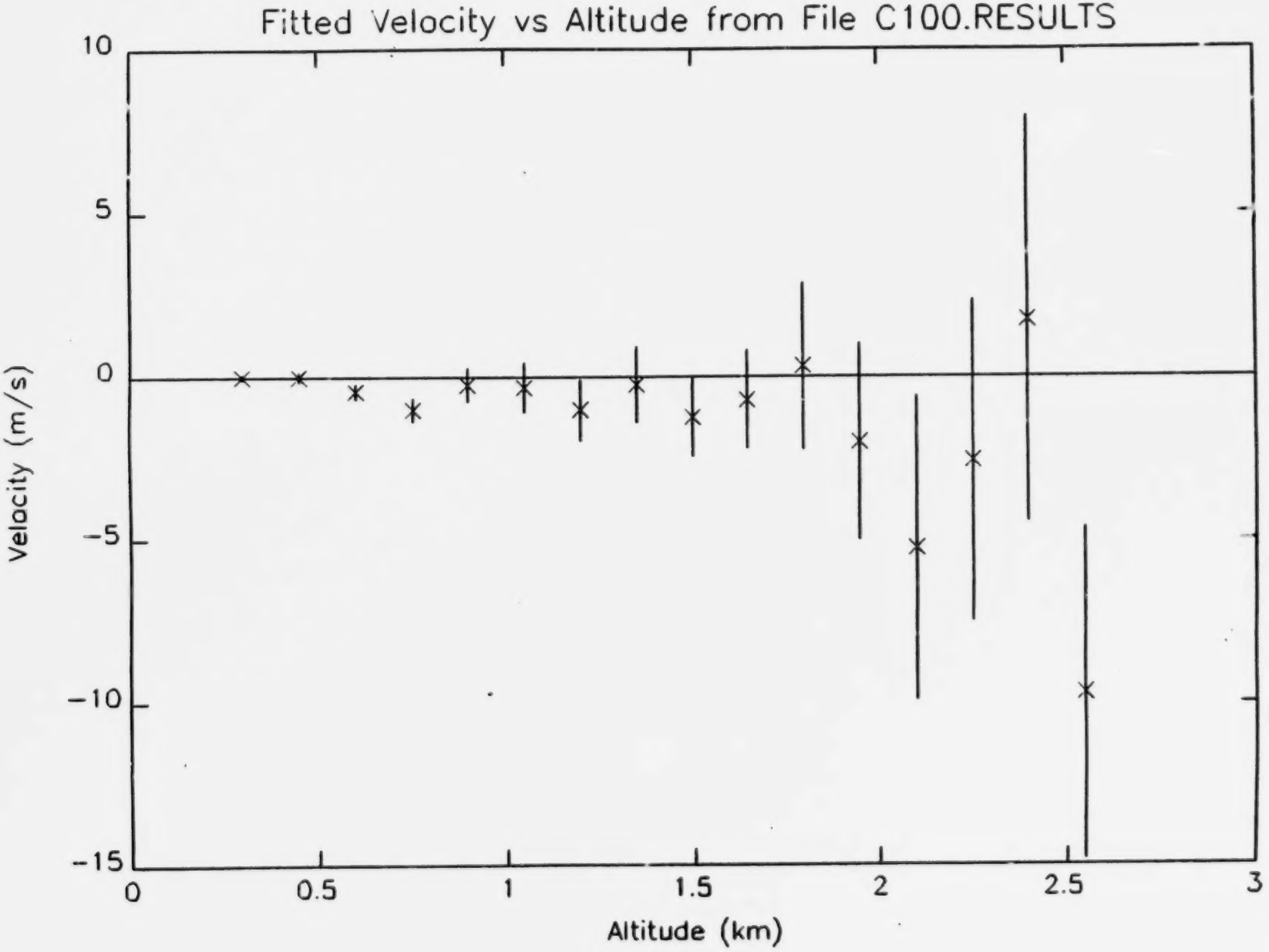
Fitted Velocity vs Altitude from File C100.RESULTS
10
5
0
-5
-10
-15
Velocity (m/s)
0
0.5
1
1.5
2
2.5
3
Altitude (km)

Figure III.5

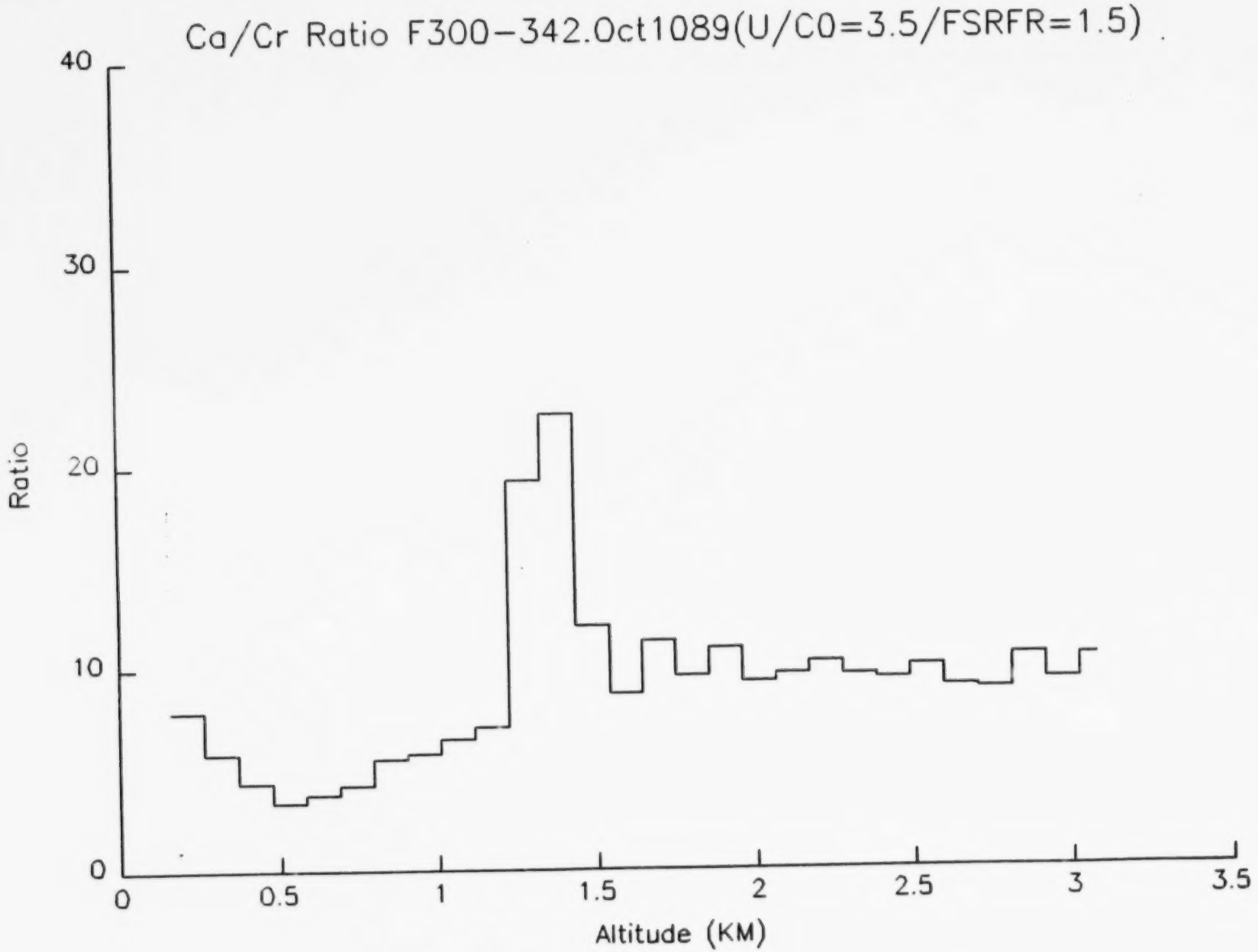
Ca/Cr Ratio F300-342.Oct1089(U/C0=3.5/FSRFR=1.5)
Ratio
40
30
20
10
0
0
0.5
1
1.5
2
2.5
3
3.5
Altitude (KM)

Figure III.6

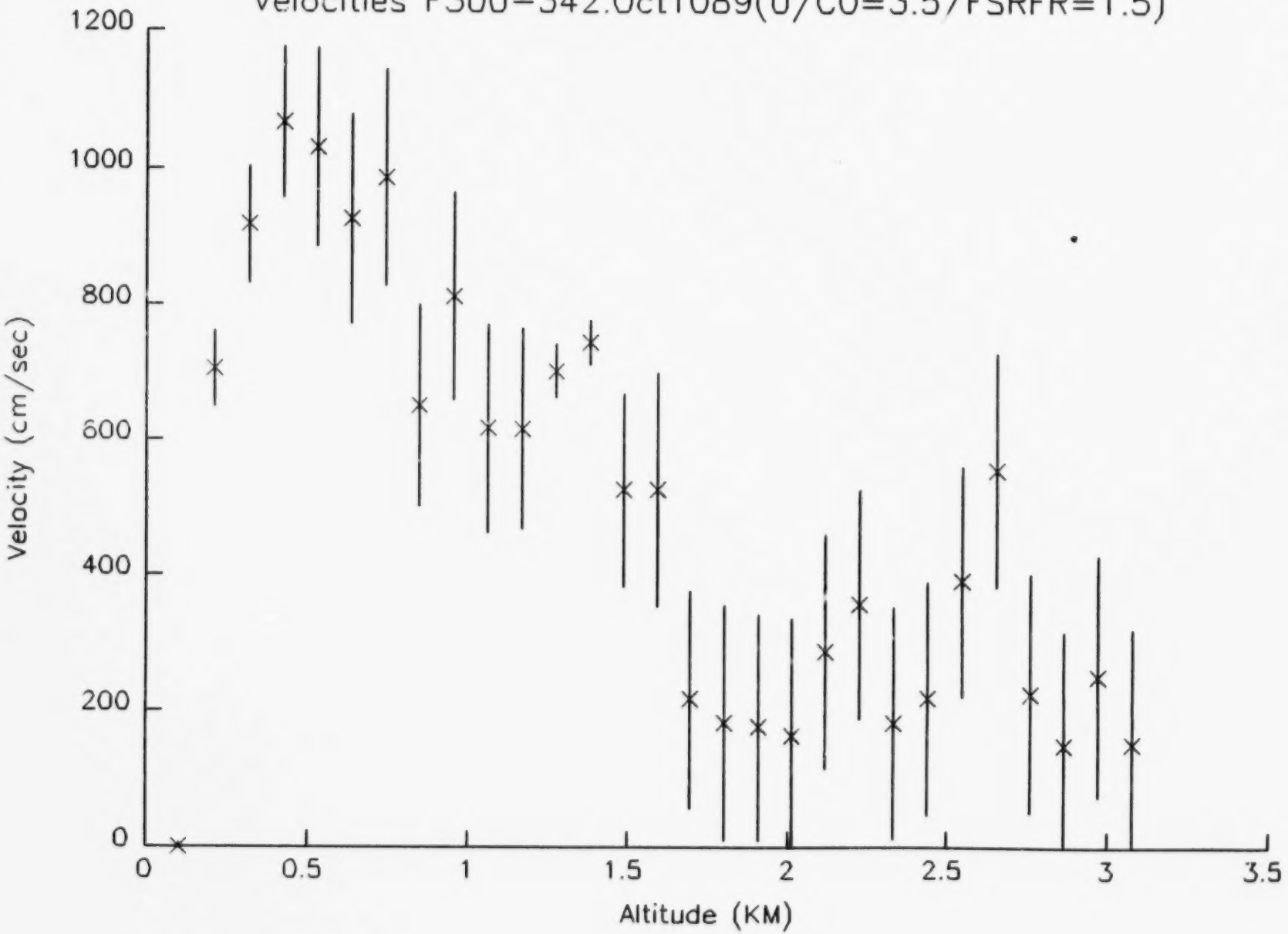
Velocities F300-342.0oct1089(U/C0=3.5/FSRFR=1.5)
Velocity (cm/sec)
1200
1000
800
600
400
200
0
0
0.5
1
1.5
2
2.5
3
3.5
Altitude (KM)

Figure III.7

Figure III.6 shows the backscattered ratio (aerosol backscattered signal/rayleigh backscattered signal) obtained October 11, 1989, at a zenith angle of 45 degrees and looking toward the east. These measurements were made with a vertical resolution of approximately 100 m, in the early evening, over a period of approximately 1/2 hour. The large ratio observed near 1.3 km is due to the presence clouds. Figure III.7 show the corresponding winds, westerly winds being positive. The winds obtained from the backscattered signal from clouds show smaller error bars. The wind velocity component observed is shown to change as a function of altitude within the boundary layer.

## *IV. SUMMARY AND RECOMMENDATIONS*

A high resolution lidar system has been implemented to measure winds in the lower atmosphere. The wind speed along the line of sight was determined by measuring the doppler shift of the aerosol backscattered laser signal. The system in its present configuration is stable, and behaves as indicated by theoretical simulations.

This system was built to demonstrate the capabilities of the detector system as a prototype for a spaceborne lidar. The detector system investigated here consisted of a plane Fabry-Perot etalon, and a 12-ring anode detector. This system is generically similar to the Fabry-Perot interferometer developed for passive wind measurements on board the Dynamics Explorer satellite. We have demonstrated that this detector system performs well in a lidar configuration.

It should be kept in mind that the detector technology used in this feasibility study is obsolete. Better Image Plane Detectors have been built, such as the one built for the High Resolution Doppler Imager to be flown on UARS, which significantly improves the accuracy of the wind measurement. Another new development is a technique for converting the circular fringes of a Fabry-Perot interferometer into a linear pattern which can be detected with a conventional linear detector. This technique, developed by (Hays, 1989) and called the Circle to Line Interferometer Optical System (CLIO), greatly simplifies the analysis of interferometric information by converting the circular rings or fringes into a linear pattern similar to that produced by a conventional spectrometer. The resulting linear fringe pattern can be scanned using any one of the many commercially available linear array detectors, a great advantage over the use of multi-ring image plane detectors that have been developed previously. The use of this device is of particular importance to a spaceborne lidar system which is concerned with optical safety, since it allows the detection of multiple order of the Fabry-Perot simultaneously, which allows an increase in the acceptance angle of the detector, and thus the divergence of the laser beam. We recommend that these new detector systems be investigated in a lidar configuration, and that further development of this spaceborne prototype system be carried out.

ORIGINAL PAGE IS
OF POOR QUALITY

## APPENDIX I

## LIDAR EQUATION WITH FABRY-PEROT DETECTOR SYSTEM

The Fabry-Perot detector system we have chosen to implement is similar to the one developed for passive wind measurements on board the Dynamics Explorer satellite. This is a stable, high resolution system consisting of a solid plane etalon and a multiring anode detector to scan spatially the plane of the Fabry-Perot. Here we will derive the mathematical function which represents the number of laser photons backscattered from the atmosphere and which are transmitted through the Fabry-Perot to the detector system.

The function used here to represent the laser lineshape is the Gaussian distribution

$$P(\lambda) = \frac{P_t}{\sqrt{\pi}\,\Delta\lambda_l} \exp\left[-\left(\frac{\lambda-\lambda_0}{\Delta\lambda_l}\right)^2\right], \qquad (1)$$

where $P_t$ is the total laser power transmitted, $\lambda_0$ is the central laser wavelength, and $\Delta\lambda_l$ is the e-folding width of the laser beam (i.e., the e-folding width is the wavelength shift at which the laser intensity has dropped to 1./e of its peak value).

The scattering cross-section can be similarly expressed by Gaussian representation of the thermal velocity distribution of the scattering medium as

$$\sigma(\lambda) = \frac{\sigma_0}{\sqrt{\pi}\,\Delta\lambda_s} \exp\left[-\left(\frac{\lambda-\lambda_v}{\Delta\lambda_s}\right)^2\right], \qquad (2)$$

where $\sigma_0$ is the Rayleigh or aerosol backscatter coefficient ($cm^2$), $\lambda_v$ is the doppler shifted reference wavelength equal to $(\lambda_0 + 2v\lambda_0/c)$, v is the velocity of the scattering media, c is the velocity of light, and $\Delta\lambda_s$ is the e-folding width of the scattering source, given by

$$\Delta\lambda_s = 4.3 \times 10^{-7}\, \lambda_0 \left(\frac{T}{M}\right)^{\frac{1}{2}},$$

where T is the temperature of the scattering media (° K), and M is the molecular weight of the scatterers in amu.

The power returned per lidar pulse $P_r(\lambda,H)$ is a convolution of the transmitted signal and the broadening function associated with the scattering media, i.e.,

$$P_r(H,\lambda) = \frac{P_t Q_0 A_0 \beta(H,\lambda)\,\Delta h q^2(H,\lambda)}{4\pi H^2} \times \frac{\exp\left[-(\lambda-\lambda_v)^2/(\Delta\lambda_1^2+\Delta\lambda_s^2)\right]}{\sqrt{\pi}\,(\Delta\lambda_1^2+\Delta\lambda_s^2)^{\frac{1}{2}}}, \tag{3}$$

where $Q_0$ is the product of the quantum and optical efficiencies, $A_0$ is the telescope area, $\beta(\lambda,H)$ is the product $N(H)\,\sigma_0(H,\lambda)$, $N(H)$ is the density of scatterers, H is the range, $\Delta h$ is the scattering layer thickness, and $Q(H,\lambda)$ is the atmospheric transmission coefficient.

The transmission through a perfect Fabry-Perot into a detector ring of width $\Delta\theta$ is given by the expression (Hays and Roble, 1971)

$$T(\lambda) = \left(\frac{1-R}{1+R}\right)\left[1 + 2\sum_{n=1}^{\infty} R^n \operatorname{sinc}\left(\frac{n\lambda_0\theta_0\Delta\theta}{\Delta\lambda}\right) \times \cos\left(2\pi n\left[\frac{\lambda-\lambda_0}{\Delta\lambda} + \frac{\lambda_0\theta_0^2}{2\Delta\lambda} + \frac{\lambda_0}{8}\frac{\Delta\theta^2}{\Delta\lambda}\right]\right)\right], \tag{4}$$

where R is the plate's reflectivity, $\Delta\lambda$ is the free spectral range, and $\theta_0$ is the angle corresponding to the average wavelength being transmitted through the ring. The width of the rings is chosen so the spatial scan is linear in wavelength. The detector system is taken into consideration by convolving equations (3) and (4). Then the number of photons detected in the jth ring is

$$N_j = \left(\frac{1-R}{1+R}\right) Q_0 C_0 \left\{ 1 + 2 \sum_{n=1}^{\infty} R^n \operatorname{sinc}\left(\frac{n\lambda_0 \theta_0 \Delta\theta}{\Delta\lambda}\right) x \right.$$

$$\left. e^{\frac{-n^2\pi^2\left(\Delta\lambda_1^2 + \Delta\lambda_s^2\right)}{\Delta\lambda^2}} \cos\left(2\pi n\left[\frac{\lambda-\lambda_0}{\Delta\lambda} + \frac{\lambda_0\theta_0^2}{2\Delta\lambda} + \frac{\lambda_0}{8}\frac{\Delta\theta^2}{\Delta\lambda}\right]\right)\right\}, \tag{5}$$

where

$$C_0 = \frac{P_t A_0 \beta(H,\lambda) \cdot \Delta h \cdot q^2(H,\lambda)\lambda_0}{4\pi H^2 hc}$$

and h is Planck's constant. This expression is a good representation of the response of an incoherent lidar which has a Fabry-Perot detector.

Next a real instrument function is used where each ring anode is expanded in a Fourier series based on the instrument calibration. The response of the instrument to backscattered laser light in the presence of a continuum background is then given by an equation similar to that described above for a perfect Fabry-Perot

$$N_j = Q_0\left(\frac{1-R}{1+R}\right)\int_0^{\infty}\left\{A_{oj} + \sum_{n=1}^{\infty}\left[A_{nj}\cos\frac{2\pi n}{\Delta\lambda}(\lambda-\lambda_0) + \right.\right.$$

$$\left.\left. B_{nj}\sin\frac{2\pi n}{\Delta\lambda}(\lambda-\lambda_0)\right]\right\}\left\{\frac{C_0 e^{-\left(\frac{\lambda-\lambda_v}{\Delta\lambda_{1+s}}\right)^2}}{\sqrt{\pi}\,\Delta\lambda_{1+s}} + B_k\right\} T_F(\lambda)\partial\lambda, \tag{6}$$

where

$$\Delta\lambda_{1+s} = (\Delta\lambda_1^2 + \Delta\lambda_s^2)^{\frac{1}{2}}.$$

Here $N_j$ is the counts recorded in the jth anode channel, $B_K$ is the continuum background intensity, and $T_f(\lambda)$ is a broadband filter transmission.

Equation (6) represents the convolution of the instrument function with a Gaussian representing the backscattered laser signal (plus background). Effecting the convolution yields

$$N_j = Q_0 T_{0F}\left(\frac{1-R}{1+R}\right)\left\{C_0 A_{0j} + C_0\left\{\sum_{n=1}^{\infty}\left[A_{nj}\cos\frac{4\pi n\nu\lambda_0}{C\Delta\lambda} + B_{nj}\sin\frac{4\pi n\nu\lambda_0}{C\Delta\lambda}\right]\right\}e^{\frac{-n^2G^2}{4}} + \frac{B_K\overline{\Delta\lambda_f}A_{0j}}{T_{0f}}\right\}, \tag{7}$$

where

$$\overline{\Delta\lambda_f} = \int_0^{\infty} T_F(\lambda)\,d\lambda \qquad G^2 = \frac{\pi^2(\Delta\lambda_1^2 + \Delta\lambda_s^2)}{\Delta\lambda^2}$$

and $T_{0F}$ is the broadband filter transmission at $\lambda_0$.

## LEAST SQUARE FITTING TECHNIQUE

The three unknowns V, $C_0$, and $B_K$ can be determined from the spectrum using a nonlinear least squares fitting technique. However, we have chosen to linearize equation (7) in order to simplify the problem to a single matrix multiplication. We thus carry out a Taylor series expansion for a function of one variable about approximated value ($V_0$) of the wind. The first order terms in the expansion are only used to obtain:

$$N_j = N_j(V_0) + \frac{\partial N_j}{\partial V}\Big|_{V_0} (V - V_0) \tag{8}$$

where

$$\frac{\partial N_j}{\partial V} = Q_0 T_{0F}\left(\frac{1-R}{1+R}\right) C_0 \sum_{n=1}^{\infty} e^{-\frac{n^2 G^2}{4}} \frac{4\pi n\lambda_0}{C\Delta\lambda}\left[A_{nj}\sin\frac{4\pi n\lambda_0 V_0}{C\Delta\lambda} - B_{nj}\cos\frac{4\pi\lambda_0 V_0}{C\Delta\lambda}\right].$$

In matrix form equation (8) can be written as

$$N_j = \sum_{k=1}^{3} A_{jk} X_k, \quad j = 1 \cdots N_{ring} \tag{9}$$

where

$$X_1 = C_0$$

$$X_2 = (V - V_0)\, C_0$$

$$X_3 = B_k.$$

The method for finding the optimum fit to the data will be to minimize the variance of the squared difference between theory and the measured spectrum with respect to the three variables defined above, that is,

$$\frac{\partial \overline{\delta N^2}}{\partial X_m} = 0, \tag{10}$$

where

$$\overline{\delta N^2} = \sum_{j=1}^{N_{ring}} W_j \left\{ N_j - \sum_{k=1}^{3} A_{jk} X_k \right\}^2$$

and $W_j$ is a weighting function. Taking the derivative of $\overline{\delta N^2}$ in equation (10) one obtains

$$\sum_{j=1}^{N_{ring}} W_j \left\{ N_j - \sum_{k=1}^{3} A_{jk} X_k \right\} A_{jk} = 0. \tag{11}$$

If we assume that the operations commute and let

$$W_j A_{jM} = S_{jM}$$

and

$$\sum_{j=1}^{N_{ring}} W_j A_{jk} A_{jM} = W_{kM},$$

the solution to equation (11) can be written as the matrix equation

$$X_k = \sum_{M=1}^{3} [W_{kM}]^{-1} \sum_{j=1}^{N_{ring}} S_{jM} N_j$$

or

$$X_k = \sum_{j=1}^{N_{ring}} C_{kj} N_j , \tag{12}$$

where $C_{kj} = \sum_{m=1}^{3} [W_{km}]^{-1} S_{jM}$ and $[\ ]^{-1}$ indicates a matrix inversion operation.

One should note that the matrices $C_{kj}(V_0)$ are dependent on the reference temperature and line of sight speed, consequently the linearization only works in the immediate vicinity of $(V_0)$. In practice, since these matrices can be precalculated, a full set of inversion matrices are computed and stored. During the data reduction process a careful initial choice is made of the starting value of $(V_0)$ and the appropriate matrix is extracted from storage and used to determine $(V_1)$ which is then used to refine the choice of $(V_0)$. If the variance of matrix choice is too large, the process is repeated until the line of sight velocity determined lies in the linear range of the inversion matrix. This process is very fast and has been used effectively in the reduction of satellite wind data from the Dynamics Explorer Fabry-Perot Interferometer (Hays et al., 1981).

This technique also has the merit of providing a simple expression for the statistical error in a given measurement set. The propagation of errors theorem for a system obeying Poisson statistics states that the standard deviations of the fitted parameters age given by

$$\sqrt{\overline{\delta X_k^2}} = \left( \sum_{j=1}^{N_{ring}} C_{kj}^2 N_j \right)^{\frac{1}{2}} . \tag{13}$$